




# Transient field-resolved reflectometry at 50–100 THz

MARCEL NEUHAUS,<sup>1,†</sup> JOHANNES SCHÖTZ,<sup>1,2,†</sup> MARIO AULICH,<sup>1</sup> ANCHIT SRIVASTAVA,<sup>1</sup> DŽIUGAS KIMBARAS,<sup>1,2</sup> VALERIE SMEJKAL,<sup>3</sup> VLADIMIR PERVAK,<sup>1</sup> MESHAA ALHARBI,<sup>4</sup> ABDALLAH M. AZZEER,<sup>4</sup> FLORIAN LIBISCH,<sup>3</sup> CHRISTOPH LEMELL,<sup>3</sup> JOACHIM BURGDÖRFER,<sup>3</sup> ZILONG WANG,<sup>1,2</sup> AND MATTHIAS F. KLING<sup>1,2,\*</sup> 

<sup>1</sup>Physics Department, Ludwig-Maximilians-Universität Munich, D-85748 Garching, Germany

<sup>2</sup>Max Planck Institute of Quantum Optics, D-85748 Garching, Germany

<sup>3</sup>Institute for Theoretical Physics, TU Wien, A-1040, Austria

<sup>4</sup>Attosecond Science Laboratory, Physics and Astronomy Department, King-Saud University, Riyadh 11451, Saudi Arabia

\*Corresponding author: matthias.kling@lmu.de

Received 13 August 2021; revised 5 November 2021; accepted 16 November 2021; published 5 January 2022

**Transient field-resolved spectroscopy enables studies of ultrafast dynamics in molecules, nanostructures, or solids with sub-cycle resolution, but previous work has so far concentrated on extracting the dielectric response at frequencies below 50 THz. Here, we implemented transient field-resolved reflectometry at 50–100 THz (3–6  $\mu\text{m}$ ) with MHz repetition rate employing 800 nm few-cycle excitation pulses that provide sub-10 fs temporal resolution. The capabilities of the technique are demonstrated in studies of ultrafast photorefractive changes in semiconductors Ge and GaAs, where the high frequency range permits to explore the resonance-free Drude response. The extended frequency range in transient field-resolved spectroscopy can further enable studies with so far inaccessible transitions, including intramolecular vibrations in a large range of systems.**

Published by The Optical Society under the terms of the [Creative Commons Attribution 4.0 License](https://creativecommons.org/licenses/by/4.0/). Further distribution of this work must maintain attribution to the author(s) and the published article's title, journal citation, and DOI.

<https://doi.org/10.1364/OPTICA.440533>

## 1. INTRODUCTION

Mid-infrared (MIR) femtosecond lasers have gained in prevalence in recent years, as they open up a variety of applications in ultrafast spectroscopy including bio-medical imaging [1,2], nonlinear optics [3,4], and nanophotonics [5]. With respect to solids, such light sources permit probing charge carrier dynamics near the band edge of low-bandgap materials [6], carrier intraband absorptions [7], and the dynamics of quasiparticles, such as plasmonic or polaron excitations [8,9]. Conventional pump-probe spectroscopy, in either transmission or reflection geometry, measures the change of the probe light amplitude before and after interacting with a sample. The phase information of the light field is thereby lost [6,10].

Both amplitude and phase information can be obtained with field-resolved spectroscopy [11–15], which records the reflected or transmitted light electric waveform [9]. There, the time resolution is not limited by the duration of the employed pump and probe pulses. It rather depends on the duration of the pump and gating pulses used to sample the field, which can both be in the visible range and have few-fs duration [15].

In attosecond spectroscopy, highly excited charge carrier dynamics in gases, nanostructures, and solids have been probed

with sub-cycle time-resolution [16,17]. Its implementation, however, required using attosecond extreme ultraviolet or x-ray pulses in a vacuum environment. This complexity has severely limited its widespread use beyond specialized laboratories, motivating the implementation of electro-optical sampling (EOS) up to optical frequencies [18].

Previous work on transient field-resolved (TFR) spectroscopy focused on extracting the dielectric response at frequencies below 50 THz [cf. Fig. 1(a)]. The frequency range above 50 THz enables access to a range of faster processes as shown in Fig. 1(a). For example, in classical semiconductors the faster tails of dynamics such as intervalley scattering [36] and polaron excitations [37], or transitions to the split-off bands [38] and the resonance-free Drude response may be investigated. In transition metal dichalcogenides (TMDs) the hot electron as well as exciton intraband dynamics can be probed [39–41]. Most prominently, the frequency range above 50 THz also contains the stretching modes of functional organic groups [42], important for bio-medical applications where they permit studies of structural dynamics [43,44] and processes such as photosynthesis [45]. In molecular/organic electronics, transfer dynamics on the few-femtosecond scale could be studied, especially at metal interfaces where an efficient transfer from the metal can be excited by the pump [46,47].

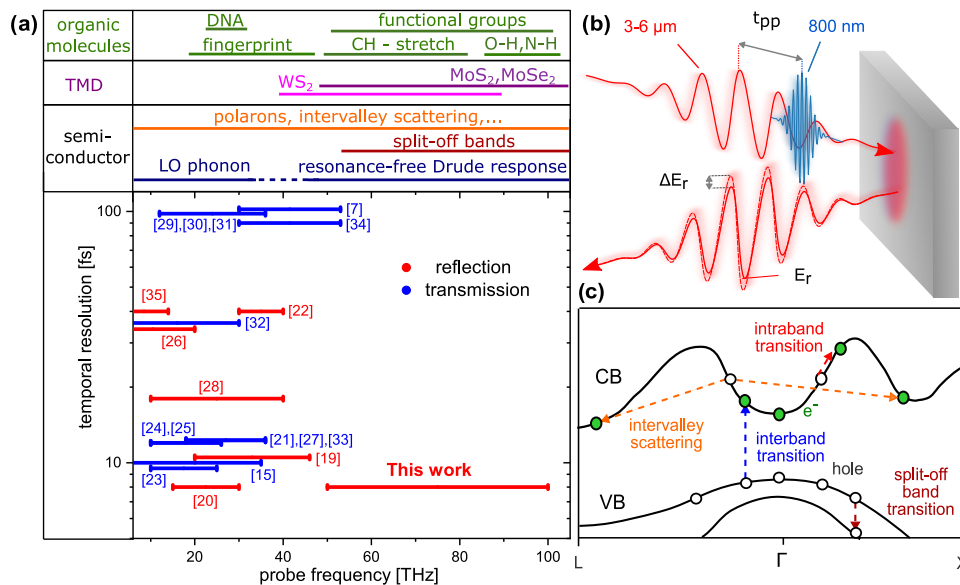


**Fig. 1.** (a) Overview of implementations of (transient) field-resolved spectroscopy above 20 THz [7,15,19–35]. On top, examples of processes that can be probed in the respective frequency range are listed. (b) Scheme for TFR reflectometry in the mid-infrared. An NIR excitation pulse (blue) induces charge carrier dynamics in the solid (depicted in gray). The unfolding dynamics leads to transient changes in the reflected waveform of the time-delayed MIR pulse (red). (c) Schematic of laser-induced processes in semiconductors (shown for the valleys in the bandstructure of Ge) that can be probed with TFR reflectometry. VB, valence band; CB, conduction band.

Here, we have developed high-repetition-rate (2.1 MHz) TFR MIR reflectometry at frequencies of 50–100 THz (3–6 μm) with sub-10 fs time resolution. The capabilities of the setup are demonstrated in ultrafast light-induced charge carrier dynamics recorded for solids, characterized through the measurement of transient changes of the MIR waveform reflected from the sample surface [cf. Fig. 1(b)]. The reflection geometry permits studies of optically thick and non-transparent samples as well as complex samples (with, e.g., non-transparent back-gating). We performed experiments at room temperature on direct (GaAs, ⟨110⟩, from Freiberger Compounds) and indirect (Ge, ⟨111⟩, from Edmund optics) bandgap semiconductors, where TFR spectroscopy allows extracting the light-induced changes of both real and imaginary parts of the material's dielectric constant. The underlying charge carrier dynamics, as, e.g., shown in Fig. 1(c), can be investigated. The near-infrared (NIR) excitation pulse induces an interband transition from a valence to a conduction band. Ultrafast carrier dynamics, such as scattering and thermalization, can be monitored via changes in the reflected MIR field induced by intraband transitions.

## 2. EXPERIMENTAL SETUP

The TFR reflectometry setup is based on a home-built non-collinear optical parametric amplifier (NOPA) driven by a high-power Ytterbium-based fiber laser (Active Fiber Systems). The NOPA delivers 2 μJ sub-8 fs pulses spanning the wavelength range 650–980 nm at a repetition rate of 2.1 MHz (see Supplement 1 for details). These pulses are used for MIR generation via intrapulse difference frequency generation (iDFG), transient excitation of the solid, and as gating pulses in EOS.

Waveform-stable, octave-spanning MIR pulses are generated via iDFG in a 1 mm thick, type-I LiIO<sub>3</sub> crystal [Fig. 2(a)] [48,49]. The LiIO<sub>3</sub> crystal is transparent in both the MIR region up to

about 6 μm and in the spectral region of the second harmonic of the driving laser. The latter is essential, as otherwise, two photon absorption of the driving pulses could damage the crystal. The driving NIR beam is focused to an intensity of 0.2 TW/cm<sup>2</sup> inside the crystal. Nonlinear distortions of the beam profile were not observed. We achieved about 1 nJ MIR pulses with more than an octave spanning bandwidth [Fig. 2(b)]. To ensure the EOS measurement fidelity of the generated MIR light, we compare results from two spectrometers (InGaAs and PbSe) as well as EOS and upconversion spectroscopy (see Supplement 1 for details) [50,51]. The spectra measured by different methods agree qualitatively well, while both nonlinear detection methods, i.e., EOS and upconversion spectroscopy, underestimate the spectral region below 3 μm due to the phase-matching in the nonlinear crystal employed in these methods. The generation and detection ranges with our setup could both be pushed down to 2 μm, but at a significant loss at long wavelengths. Since the setup is operated under ambient conditions, CO<sub>2</sub> absorption at 4.2 μm is apparent but could be removed by purging. We note, however, that the exact spectral shape is not crucial, as TFR spectroscopy detects only relative changes.

The MIR and NIR beams after the iDFG crystal are separated using a 1 mm thick silicon plate under the Brewster angle for the MIR. The reflected NIR radiation is further divided into two arms by a 50:50 beam splitter [Fig. 2(a)]. One arm serves as a pump beam for the sample, and the other serves as an EOS gating pulse. Both the NIR pump and MIR probe are focused onto the sample by a spherical concave mirror under a small angle below 5° to the surface normal to separate the in- and outgoing beams. The reflected MIR probe beam is then re-combined with the EOS gating pulse using another silicon plate and focused into a 0.2 mm thick LiIO<sub>3</sub> crystal for EOS detection of the MIR electric field [18]. The polarization rotation of the spectrally selected sum-frequency generation (SFG) signal induced by the gate pulse, in a band of 680–720 nm that gave the best signal-to-noise,

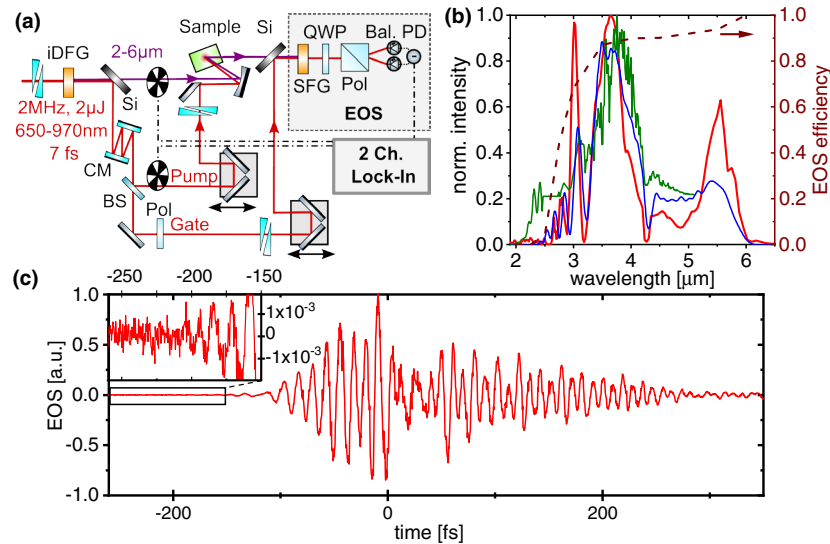


**Fig. 2.** (a) Setup for TFR-MIR reflectometry. HWP, half-wave plate; QWP, quarter-wave plate; BS, beam splitter; Pol, polarizer; Si, silicon plate; CM, chirped mirrors. (b) MIR spectrum measured with EOS (red), upconversion spectroscopy (blue), and commercial spectrometers (green; see Supplement 1 for details). The dashed red line shows the simulated relative EOS response function. The dip at 4.2  $\mu\text{m}$  is due to  $\text{CO}_2$  absorption. (c) Electric field recorded by EOS. The inset shows the magnification of the EOS signal from the leading edge of the MIR field, indicating a measurement noise floor of less than  $10^{-3}$ . Signals after 300 fs originate from the free-induction decay induced by absorption of  $\text{CO}_2$  and  $\text{LiIO}_3$ .

was detected using balanced photodiodes after a quarter-wave plate and a Wollaston prism [Fig. 2(a)]. The time domain MIR waveform is obtained by scanning the relative time delay,  $t_{\text{EOS}}$ , between the MIR and EOS gating pulses. The pump-induced MIR waveform changes are obtained by acquiring the waveform for varying pump-probe delays  $t_{\text{pp}}$ . A typical MIR spectrum and the corresponding waveform are shown in Figs. 2(b) and 2(c). The small field oscillations below  $2 \cdot 10^{-3}$  at the leading edge of the MIR field can be clearly seen in the inset of Fig. 2(c). The noise floor is well below  $1 \cdot 10^{-3}$ , which makes the setup sensitive enough for detecting small changes upon photoexcitations of the sample. The EOS traces were recorded with a typical measurement time of 30–60 s per EOS trace or about 0.2 s per measurement point.

We use a dual-modulation technique with two optical choppers to achieve the high sensitivity in the measurements. We modulate the MIR probe at a frequency of  $f_0 = 1.5$  kHz and the pump at  $f_{\Delta} = 5.7$  kHz. The measured EOS signal, at each pump-probe delay, is then de-modulated using a two-channel lock-in amplifier. The electric field of the reflected probe beam without the pump,

$E_r$ , can be measured at the reference frequency  $f_0$ . At the same time, the pump-induced electric field change of the reflected MIR probe beam,  $\Delta E_r$ , is measured at the reference frequency  $f_{\Delta}$  (see Supplement 1). By comparing these two, the influence of drifts in the path length of the EOS interferometer as well as of laser power fluctuations on the measurement can be suppressed. This technique offers another large advantage for stretched MIR pulses. It is known that for temporally stretched MIR pulses and an uneven spectral response of the EOS, temporally varying phase distortions between the MIR field and EOS can occur and distort the measurement [52,53]. However, as we measure  $E_r$  and  $\Delta E_r$  with the same detector, these phase distortions are equally present in both signals, and no relative phase distortion is observed, as could also be verified by simulations (cf. Supplement 1).

### 3. RESULTS AND DISCUSSION

Figure 3(a) shows typical time domain signals of the reflected MIR field without a pump [ $E_r(t)$ , blue circles] and the pump-induced

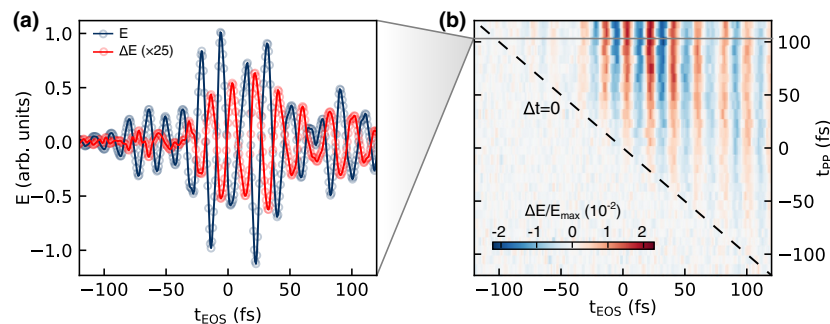


**Fig. 3.** Experimental signal: (a) EOS measurement of the reflected field (blue circles) and the pump-field-induced change (red circles) on GaAs for a fixed pump-probe delay of about 100 fs (positive delays correspond to the pump arriving before the probe). The solid lines are obtained by Fourier-filtering out wavelength components below 1.2  $\mu\text{m}$  and above 14  $\mu\text{m}$ , lying outside the MIR spectrum. (b) Pump-probe delay ( $t_{\text{pp}}$ ) resolved relative change of the reflected field  $\Delta E_r/E_{r,\text{max}}$ , where  $E_{r,\text{max}}$  is the maximum field strength. The diagonal (dashed line) indicates the propagation of the pump pulse through the EOS sampling window.

change of the reflected field [ $\Delta E_r(t)$ , red circles] at a fixed pump–probe delay of about 100 fs from a GaAs sample. The measured  $\Delta E_r(t)$  is out of phase with  $E_r(t)$  by  $\pi$ , indicating a reduced reflectivity after the NIR pump excitation. Figure 3(b) shows a 2D plot of the TFR measurement of the change of the reflected field normalized to the maximum of the reflected field without a pump,  $\Delta E_r(t)/E_{r,\max}$ , at each pump–probe delay. The dashed diagonal line marks the simultaneous arrival time of the NIR pump and MIR probe pulses ( $\Delta t_{pp} = 0$ ). Changes in  $\Delta E_r$  appear for  $\Delta t_{pp} > 0$  within tens of femtoseconds. The time resolution of the TFR experiments is limited only by the duration of the sub-10 fs NIR pulse used as an excitation and EOS gate pulse [16,53,54].

The relative change of the reflection coefficient in the frequency domain,  $\Delta r(\omega)/r(\omega)$ , can be calculated by Fourier transforming the measured time domain signals:

$$\frac{\Delta r(\omega)}{r(\omega)} = \frac{\Delta E_r(\omega)}{E_r(\omega)} = \left| \frac{\Delta E_r(\omega)}{E_r(\omega)} \right| e^{i\Delta\phi(\omega)}, \quad (1)$$

where  $r$  is the reflection coefficient for the amplitude of the electric field without a pump, and  $\Delta\phi(\omega)$  is the pump-induced phase shift in the frequency domain. Its spectral derivative,  $d\Delta\phi(\omega)/d\omega$ , determines the contribution to the group delay  $\Delta\tau_g$  for backscattering induced by the electronic excitation of the medium. As the electronic excitation will relax and diffuse, this group delay contribution  $\Delta\tau_g(t_{pp})$  will be a function of the pump–probe delay and offers the opportunity to investigate transport and decoherence in the medium on femto- to picosecond time scales. The relative reflectivity change of the sample,  $\Delta R/R$ , can be worked out from the change of the sample reflectivity  $\Delta R = |r + \Delta r|^2 - |r|^2$ :

$$\frac{\Delta R}{R} = 2\text{Re}\left(\frac{\Delta r}{r}\right) + \text{Re}\left(\frac{\Delta r}{r}\right)^2 + \text{Im}\left(\frac{\Delta r}{r}\right)^2, \quad (2)$$

where Re and Im are the real and imaginary parts of the complex relative change of the reflection coefficient, respectively. For small changes in reflectivity, intensity-resolved measurements are considerably less sensitive to the imaginary part compared to the TFR approach. The pump-induced change in reflectivity  $\Delta r$  is linked to the change in refractive index,  $\Delta n$ , through Fresnel equations (see Supplement 1 for details):

$$\Delta r \approx \frac{-2\Delta n}{(1+n)^2}, \quad (3)$$

where  $n$  is the refractive index of the unexcited sample. The change of permittivity is then given by  $\Delta\epsilon = (n + \Delta n)^2 - n^2$ . We then can directly link the changes in reflectivity and permittivity:

$$\Delta r \approx \frac{-\Delta\epsilon}{n(1+n)^2}. \quad (4)$$

This can be compared to the theoretic prediction of  $\Delta\epsilon$  after the excitation of carriers by the pump pulse. In a first approximation, the intraband charge carrier dynamics driven by the probe pulse may be modeled using the Drude function, assuming the measured change in the refractive index arises from free-carrier dynamics:

$$\Delta\epsilon_k = \frac{-n_{fc,k} \cdot e^2}{m_{eff,k} \cdot \epsilon_0} \cdot \frac{1}{\omega^2 - i\omega\Gamma_k}, \quad (5)$$

with  $n_{fc}$  the free-carrier density,  $e$  the electron charge,  $m_{eff}$  the charge carrier effective mass,  $\Gamma$  the Drude scattering rate (i.e., momentum relaxation rate) in the corresponding band, and  $\epsilon_0$  the vacuum permittivity. The index  $k$  labels the band and, for electrons, the valley they are moving in. Considering that the pump-induced carriers by far exceed the intrinsic ones, and neglecting bandgap renormalization, the total pump-induced change of the frequency-dependent dielectric function is  $\Delta\epsilon(\omega, t_{pp}) = \sum_k \Delta\epsilon_k$ . The latter depends on the pump–probe delay  $t_{pp}$ .

The spectral region of the probe light in the experiment is far away from the plasma frequency  $\omega_{pl}$  associated with the free-carrier density at the employed pump fluence of  $400 \mu\text{Jcm}^{-2}$ – $400 \mu\text{Jcm}^{-2}$ . Therefore, the variation of  $\Delta r(\omega)$  across the spectral window of the MIR probe is smooth and does not contain the plasmon resonance peak. More importantly, our probe frequency region is also free of phonon-absorption features in semiconductors which otherwise might affect the observed dynamics. The pump–probe delay time  $t_{pp}$  dependence of the transient reflectivity change in GaAs integrated over the spectral window (3.5–6.4)  $\mu\text{m}$ , cf. Figure 4(a), displays a finite rise time of the signal with  $\tau_{rise} = 82$  fs as fitted by a Fermi function. The delay shown here corresponds to a delay parallel to the diagonal shown in Fig. 3(b) to compensate for the different pump arrival times for different MIR-field components [55]. A closer look at the spectral response of the signal [Fig. 4(b)] at small pump–probe delays ( $t_{pp} = 12$  fs) and later time delays ( $t_{pp} = 175$  fs), when the buildup is complete, reveals information on the temporal evolution of the response. It proceeds from an initially rather flat

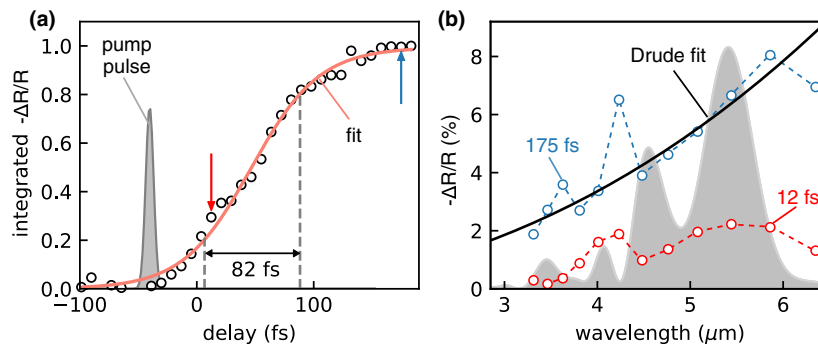


**Fig. 4.** Buildup of the reflectivity change in GaAs: (a) normalized measured relative reflectivity change (dots) integrated over the wavelength range 3.5–6.4  $\mu\text{m}$  and fitted to a Fermi function (red). Dashed lines indicate the rise time of 82 fs from 20% to 80% of the saturation level. (b) Wavelength-resolved  $\Delta R/R$  for a delay of 12 fs (red dots and dashed line) and 175 fs (blue dots and dashed line). The two delays are indicated by arrows in (a). For the latter delay, the calculated Drude expression is also shown (black solid line), which yields an excited carrier density of  $1.2 \cdot 10^{18} \text{ cm}^{-3}$  and a plasma oscillation period of  $\sim 60$  fs.

spectral response at short times to a Drude shape in the homogeneous approximation [Eq. (5)]. Overall, both spectra exhibit a smooth shape, as expected, with the exception of the sharp peak at  $4.2 \mu\text{m}$  due to  $\text{CO}_2$  absorption. The finite response time [Fig. 4(a)] directly reflects the buildup of a Drude-type free-carrier response upon NIR photoexcitation with an excited carrier density of  $1.2 \cdot 10^{18} \text{cm}^{-3}$  as determined from the Drude fit [cf. Fig. 4(b)]. Invoking the theory for the time-resolved buildup of structured continua [56,57] with frequency-dependent probabilities

$$P(\omega, t) = \left| 1 + (i - q) \frac{\Gamma}{2} \frac{\exp[i(\omega_{\text{pl}} - i\Gamma/2 - \omega)t] - 1}{\omega - (\omega_{\text{pl}} - i\Gamma/2)} \right|^2, \quad (6)$$

( $q$ : Fano asymmetry parameter), the rise time  $\tau_{\text{rise}}$  should, in the present case, be determined by the total decay width (or scattering rate  $\Gamma$ ),  $\tau_s = 1/\Gamma$ . Our result of  $\tau_s = 85 \text{fs}$  is consistent with the Drude scattering time found in [15] and the present value of  $\tau_{\text{rise}}$ . We thus interpret the results of Fig. 4 as an experimental verification of the time resolved buildup of a structured continuum involving free carriers in a solid. Previously, the buildup of Fano-type resonances was observed only for atomic helium in the gas phase [58,59].

Different from GaAs, we observe the buildup of changes in the reflectivity of Ge on a much longer time scale extending to  $\sim 3 \text{ps}$  [Fig. 5(a)]. This can be understood in terms of the different band structures and, subsequently, the different charge carrier dynamics of the two samples. GaAs has a direct bandgap where the NIR pump, in the range of  $1.2\text{--}1.9 \text{eV}$ , excites charge carriers from the top of the valence band into the bottom of the conduction band around the  $\Gamma$ -point. The photo-induced charge carriers are expected to scatter and to relax within this  $\Gamma$ -valley

before recombining with the hole since other valleys, e.g., L- and X-valleys, lie at much higher band energies.

In contrast, Ge has an indirect bandgap and the interband transition occurs away from the high symmetry valleys [Fig. 5(b)]. Intervalley scattering of photoexcited electrons in the conduction band plays therefore a major role in the carrier dynamics on the femto- to picosecond time scale. Indeed, Monte Carlo simulations [60,61] reveal the contributions of scattering among  $\Gamma$ -, X-, and L-valleys to the buildup of reflectivity. The long rise time of the signal corresponds mostly to the conduction band filling of the L-valley within  $4\text{--}5 \text{ps}$ .

We could reproduce the rise of transient reflectivity by inserting the extracted time-dependent conduction band valley populations [Fig. 5(c)] with their transverse effective masses (see Supplement 1) into a sum of Drude terms [Eq. (5)] of the  $\Gamma$ -, X-, and L-valleys [Fig. 5(d)]. The results agree qualitatively well with measured traces, except for the sharp peak at around  $50 \text{fs}$ , which results from the strong contribution of  $\Gamma$ -valley scattering due to excitation higher in the band where the band can no longer be approximated as parabolic. Therefore, the effective mass approximation is not valid anymore. Overall, the different buildup behavior observed for GaAs and Ge can be well explained using the Drude model when accounting for the different effective masses of the electrons in different valleys. On much longer time scales, the relaxation processes in both GaAs and Ge behave identically exhibiting a typical time constant of  $20 \text{ps}$  for the data fitted up to  $80 \text{ps}$  [inset of Fig. 5(a)].

Additional interesting insights can be gained from the separate observation of the time evolution of the imaginary and real parts of the relative reflectivity change  $\Delta r/r$  as shown in Fig. 5(e). The magnitude of the real part (blue open dots) keeps rising after a

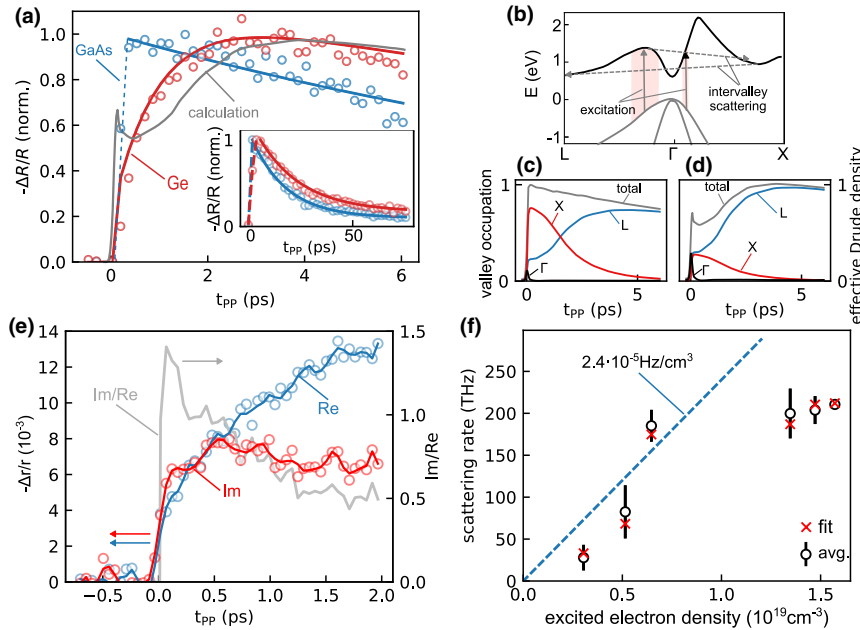


**Fig. 5.** Intervalley scattering in Ge: (a) normalized rise in reflectivity change in Ge (red dots) compared to GaAs (blue dots) with double-exponential fit (solid line). The gray line shows the calculated Drude reflectivity change based on the evolution of the conduction band valley occupations simulated in [60] for an excitation with  $\hbar\omega = 1.5 \text{eV}$  and the effective masses from [61]. Inset: long-term evolution. (b) Schematic overview of the excited electron dynamics in the band structure after photo-excitation. (c) Occupation of the individual conduction band valleys, extracted from [60] assuming a recombination time constant of  $20 \text{ps}$ . (d) Individual valley contribution to the effective Drude density (carrier density divided by relative transverse effective mass) calculated from the valley occupation in (c). (e) Typical evolution of the real (blue) and imaginary parts (red) of the reflectivity change in Ge at  $5 \mu\text{m}$ . The ratio of  $\text{Im}/\text{Re}[(\Delta r/r)]$  is shown in gray on the right axis. (f) Dependence of effective Drude scattering rates on the Drude density obtained for wavelengths between  $4.5\text{--}5.5 \mu\text{m}$  (black bars) and from a Drude fit (red crosses).

sharp initial increase around  $t_{pp} = 0$ , while the imaginary part (red open dots) quickly flattens and even starts to decrease after 500 fs of delay. Within the Drude model [Eq. (5)], assuming a homogeneously excited sample, the ratio between the imaginary and real parts of the reflection amplitude can be approximated for small changes in the refractive index to leading order by

$$\frac{\text{Im}(\Delta r/r)}{\text{Re}(\Delta r/r)} \approx \frac{\Gamma}{\omega}, \quad (7)$$

assuming that the unperturbed refractive index,  $n$ , is real valued, which applies to our case. While the effective Drude density defined as the carrier density divided by the relative transverse effective mass  $n_k/m_k$ , and thus  $\Delta r/r$ , increases through intervalley scattering, the ratio in Eq. (7) is initially approximately constant until the time-dependent effective scattering rate  $\Gamma$  starts to decrease after about 200 fs. At the high excitation densities of our experiment, carrier–carrier scattering is the major contribution [62,63]. However, the scattering time also depends on the carrier distribution since, for carriers excited far above the band valley, carrier–phonon scattering is significantly increased [64]. The subsequently reduced Drude scattering rate arises from the decreased carrier–carrier interactions when the electrons are scattered into different valleys as well as the reduction of the carrier–phonon scattering as the excited carrier distribution thermalizes and relaxes.

The dependence of the Drude scattering on the excited carrier density and thus the carrier–carrier scattering rate can be probed by measurement of the pump–intensity dependence of  $\Gamma$  for varying pump–probe delays. The extracted Drude scattering rate for different free-carrier densities, evaluated at  $t_{pp} = 1.5$  ps, when most of the density is in the L-valley, is shown in Fig. 5(f). The NIR pump pulse is absorbed by the Ge sample within a sub-micrometer length scale. The MIR probe pulse is transmitted through the medium without considerable absorption and experiences a spatially decaying excited electron distribution. Therefore, the scattering rate and electron densities need to be corrected for different penetration depths of the MIR and NIR pulses into the material (e.g., [62]). Our approach based on transfer-matrix calculations is described in Supplement 1. The retrieved scattering rate increases approximately linearly with the free-carrier density for densities  $0.5 - 1 \cdot 10^{19} \text{ cm}^{-3}$  as indicated by the blue dashed line. At higher excitation density,  $\Gamma$  appears to saturate, which may be an indication of the reduced available final states for e-e, e-h, and h-h scattering [65]. The high scattering rates of the order of  $\sim 100$  THz, corresponding to a Drude scattering time of  $\tau_s \approx 10$  fs, also have important implications for ultrafast strong-field processes in solids. Most prominently, the efficient generation of high harmonics [4] in dielectrics involves the acceleration of a coherently driven electronic wave packet in the conduction band and its eventual recombination with the hole. Electron–phonon and electron–electron (and hole) scattering is the main source for the decoherence of this process [66,67]. Independent determination of Drude scattering rates from the complex reflection and transmission amplitudes thus promises novel insights into such decohering processes on the femtosecond scale.

#### 4. CONCLUSION

We have demonstrated field-resolved transient reflectometry in the short-wavelength MIR region above 50 THz. The approach

permits recording ultrafast dynamics in molecules, nanostructures, and solids with temporal resolutions reaching 8 fs at MHz repetition rates. The temporal evolution of the change in the reflected field's amplitude and phase can be obtained, simultaneously providing access to the pump-induced real and imaginary parts of the refractive index change of the material.

We have shown the capabilities of the technique and its extended frequency range in measurements of charge carrier dynamics in classical semiconductors Ge and GaAs. In GaAs, we could observe a buildup of the resonance-free Drude response within 82 fs. In Ge, the real and imaginary parts of the reflectivity indicate a time-dependent Drude scattering rate due to a reduction of many-body carrier–carrier interactions following intervalley scattering.

In the future, the achievable intensity (up to  $\text{TW cm}^{-2}$ ) of NIR pump pulses will also allow for nonlinear excitations in the sample. The demonstrated field-resolved transient reflectometry at frequencies of 50–100 THz paves the way towards studies involving intramolecular vibrational transitions in a wide range of systems, including in molecular/organic electronics.

**Funding.** Technische Universität Wien (doctoral college TU-D); Max-Planck-Gesellschaft (IMPRS-APS, Max Planck Fellow program, MPSP); Austrian Science Fund (W1243 “Solids4Fun”); Alexander von Humboldt-Stiftung; European Research Council (COFUND Multiply, COST Action CA18234, FETopen PetaCOM); Deutsche Forschungsgemeinschaft (LMUexcellent, SFB1375).

**Acknowledgment.** We are grateful to Ferenc Krausz for his support and for providing suitable laboratory space. We acknowledge fruitful discussions with Rupert Huber, Thomas Nubbemeyer, and Shubhadeep Biswas, and early contributions to the design of the system by Pawel Wnuk. Z.W. acknowledges support by the Alexander von Humboldt Foundation. J.S. and V.S. are grateful for support by the International Max Planck Research School on Advanced Photon Science (IMPRS-APS). D.K. and M.F.K. acknowledge support by the Max Planck School of Photonics (MPSP). M.A. and A.M.A. are grateful for support by the Researchers Supporting Project RSP-2021/152, King Saud University, Riyadh, Saudi Arabia.

**Disclosures.** The authors declare no conflicts of interest.

**Data availability.** The data will be provided upon reasonable request from the authors.

**Supplemental document.** See Supplement 1 for supporting content.

<sup>†</sup>These authors contributed equally to this work.

#### REFERENCES

1. I. Pupeza, M. Huber, M. Trubetskov, W. Schweinberger, S. A. Hussain, C. Hofer, K. Fritsch, M. Poetzlberger, L. Vamos, E. Fill, T. Amotchkina, K. V. Kepesidis, A. Apolonski, N. Karpowicz, V. Pervak, O. Pronin, F. Fleischmann, A. Azzeer, M. Žigman, and F. Krausz, “Field-resolved infrared spectroscopy of biological systems,” *Nature* **577**, 52–59 (2020).
2. S. Türker-Kaya and C. W. Huck, “A review of mid-infrared and near-infrared imaging: principles, concepts and applications in plant tissue analysis,” *Molecules* **22**, 168 (2017).
3. J. Pupekis, P.-A. Chevreuil, N. Bigler, L. Gallmann, C. R. Phillips, and U. Keller, “Water window soft x-ray source enabled by a 25 w few-cycle 2.2  $\mu\text{m}$  OPCPA at 100 khz,” *Optica* **7**, 168–171 (2020).
4. S. Ghimire and D. Reis, “High-harmonic generation from solids,” *Nat. Phys.* **15**, 10–16 (2019).
5. H. Guo, W. Weng, J. Liu, F. Yang, W. Hänsel, C. S. Brès, L. Thévenaz, R. Holzwarth, and T. J. Kippenberg, “Nanophotonic supercontinuum-based mid-infrared dual-comb spectroscopy,” *Optica* **7**, 1181–1188 (2020).
6. Y. Aytac, M. Mittendorff, and T. E. Murphy, “Probing the free-carrier absorption in multi-layer black phosphorus,” *Appl. Phys. Lett.* **113**, 031108 (2018).

7. P. Steinleitner, P. Merkl, P. Nagler, J. Mornhinweg, C. Schüller, T. Korn, A. Chernikov, and R. Huber, "Direct observation of ultrafast exciton formation in a monolayer of  $\text{WSe}_2$ ," *Nano Lett.* **17**, 1455–1460 (2017).
8. Y. Zhong, S. D. Malagari, T. Hamilton, and D. M. Wasserman, "Review of mid-infrared plasmonic materials," *J. Nanophoton.* **9**, 093791 (2015).
9. E. Cinquanta, D. Meggiolaro, S. G. Motti, M. Gandini, M. J. P. Alcocer, Q. A. Akkerman, C. Vozzi, L. Manna, F. De Angelis, A. Petrozza, and S. Stagira, "Ultrafast THz probe of photoinduced polarons in lead-halide perovskites," *Phys. Rev. Lett.* **122**, 166601 (2019).
10. T.-T. Yeh, H. Shirai, C.-M. Tu, T. Fujii, T. Kobayashi, and C.-W. Luo, "Ultrafast carrier dynamics in Ge by ultra-broadband mid-infrared probe spectroscopy," *Sci. Rep.* **7**, 40492 (2017).
11. A. Leitenstorfer, S. Hunsche, J. Shah, M. C. Nuss, and W. H. Knox, "Detectors and sources for ultrabroadband electro-optic sampling: experiment and theory," *Appl. Phys. Lett.* **74**, 1516–1518 (1999).
12. H. Y. Hwang, S. Fleischer, N. C. Brandt, B. G. Perkins, Jr., M. Liu, K. Fan, A. Sternbach, X. Zhang, R. D. Averitt, and K. A. Nelson, "A review of non-linear terahertz spectroscopy with ultrashort tabletop-laser pulses," *J. Mod. Opt.* **62**, 1447–1479 (2015).
13. R. Ulbricht, E. Hendry, J. Shan, T. F. Heinz, and M. Bonn, "Carrier dynamics in semiconductors studied with time-resolved terahertz spectroscopy," *Rev. Mod. Phys.* **83**, 543 (2011).
14. A. Pashkin, M. Kempa, H. Němec, F. Kadlec, and P. Kužel, "Phase-sensitive time-domain terahertz reflection spectroscopy," *Rev. Sci. Instrum.* **74**, 4711–4717 (2003).
15. R. Huber, F. Tauser, A. Brodschelm, M. Bichler, G. Abstreiter, and A. Leitenstorfer, "How many-particle interactions develop after ultrafast excitation of an electron-hole plasma," *Nature* **414**, 286–289 (2001).
16. S. R. Leone and D. M. Neumark, "Attosecond science in atomic, molecular, and condensed matter physics," *Faraday Discuss.* **194**, 15–39 (2016).
17. F. Schlaepfer, M. Lucchini, S. A. Sato, M. Volkov, L. Kasmi, N. Hartmann, A. Rubio, L. Gallmann, and U. Keller, "Attosecond optical-field-enhanced carrier injection into the GaAs conduction band," *Nat. Phys.* **14**, 560–564 (2018).
18. S. Keiber, S. Sederberg, A. Schwarz, M. Trubetskov, V. Pervak, F. Krausz, and N. Karpowicz, "Electro-optic sampling of near-infrared waveforms," *Nat. Photonics* **10**, 159–162 (2016).
19. M. Eisele, T. L. Cocker, M. A. Huber, M. Plankl, L. Viti, D. Ercolani, L. Sorba, M. S. Vitiello, and R. Huber, "Ultrafast multi-terahertz nano-spectroscopy with sub-cycle temporal resolution," *Nat. Photonics* **8**, 841–845 (2014).
20. M. P. Fischer, C. Schmidt, E. Sakat, J. Stock, A. Samarelli, J. Frigerio, M. Ortolani, D. J. Paul, G. Isella, A. Leitenstorfer, P. Biagioni, and D. Brida, "Optical activation of germanium plasmonic antennas in the mid-infrared," *Phys. Rev. Lett.* **117**, 047401 (2016).
21. G. Günter, A. A. Anappara, J. Hees, A. Sell, G. Biasiol, L. Sorba, S. De Liberato, C. Ciuti, A. Tredicucci, A. Leitenstorfer, and R. Huber, "Sub-cycle switch-on of ultrastrong light-matter interaction," *Nature* **458**, 178–181 (2009).
22. M. A. Huber, M. Plankl, M. Eisele, R. E. Marvel, F. Sandner, T. Korn, C. Schüller, R. F. Haglund, R. Huber, and T. L. Cocker, "Ultrafast mid-infrared nanoscopy of strained vanadium dioxide nanobeams," *Nano Lett.* **16**, 1421–1427 (2016).
23. R. Huber, C. Kübler, S. Tübel, A. Leitenstorfer, Q. Vu, H. Haug, F. Köhler, and M.-C. Amann, "Femtosecond formation of coupled phonon-plasmon modes in InP: ultrabroadband THz experiment and quantum kinetic theory," *Phys. Rev. Lett.* **94**, 027401 (2005).
24. K. W. Kim, A. Pashkin, H. Schöfer, M. Beyer, M. Porer, T. Wolf, C. Bernhard, J. Demsar, R. Huber, and A. Leitenstorfer, "Ultrafast transient generation of spin-density-wave order in the normal state of  $\text{BaFe}_2\text{As}_2$  driven by coherent lattice vibrations," *Nat. Mater.* **11**, 497–501 (2012).
25. C. Kübler, H. Ehrke, R. Huber, R. Lopez, A. Halabica, R. F. Haglund, and A. Leitenstorfer, "Coherent structural dynamics and electronic correlations during an ultrafast insulator-to-metal phase transition in  $\text{VO}_2$ ," *Phys. Rev. Lett.* **99**, 116401 (2007).
26. Y. Lan, B. J. Dringoli, D. A. Valverde-Chávez, C. S. Ponceca, M. Sutton, Y. He, M. G. Kanatzidis, and D. G. Cooke, "Ultrafast correlated charge and lattice motion in a hybrid metal halide perovskite," *Sci. Adv.* **5**, eaaw5558 (2019).
27. S. Leinß, T. Kampfrath, K. V. Volkman, M. Wolf, J. T. Steiner, M. Kira, S. W. Koch, A. Leitenstorfer, and R. Huber, "Terahertz coherent control of optically dark paraexcitons in  $\text{Cu}_2\text{O}$ ," *Phys. Rev. Lett.* **101**, 246401 (2008).
28. B. Mayer, C. Schmidt, J. Bühler, D. V. Seletskiy, D. Brida, A. Pashkin, and A. Leitenstorfer, "Sub-cycle slicing of phase-locked and intense mid-infrared transients," *New J. Phys.* **16**, 063033 (2014).
29. P. Merkl, F. Mooshammer, P. Steinleitner, A. Girnghuber, K. Q. Lin, P. Nagler, J. Holler, C. Schüller, J. M. Lupton, T. Korn, S. Ovesen, S. Brem, E. Malic, and R. Huber, "Ultrafast transition between exciton phases in van der Waals heterostructures," *Nat. Mater.* **18**, 691–696 (2019).
30. P. Merkl, F. Mooshammer, S. Brem, A. Girnghuber, K.-Q. Lin, L. Weigl, M. Liebich, C.-K. Yong, R. Gillen, J. Maultzsch, J. M. Lupton, E. Malic, and R. Huber, "Twist-tailoring coulomb correlations in van der Waals homobilayers," *Nat. Commun.* **11**, 2167 (2020).
31. P. Merkl, C.-K. Yong, M. Liebich, I. Hofmeister, G. Berghäuser, E. Malic, and R. Huber, "Proximity control of interlayer exciton-phonon hybridization in van der Waals heterostructures," *Nat. Commun.* **12**, 1719 (2021).
32. M. R. Otto, L. P. René de Cotret, D. A. Valverde-Chavez, K. L. Tiwari, N. Émond, M. Chaker, D. G. Cooke, and B. J. Siwick, "How optical excitation controls the structure and properties of vanadium dioxide," *Proc. Natl. Acad. Sci. USA* **116**, 450–455 (2019).
33. M. Porer, J. M. Ménard, A. Leitenstorfer, R. Huber, R. Degl'Innocenti, S. Zanotto, G. Biasiol, L. Sorba, and A. Tredicucci, "Nonadiabatic switching of a photonic band structure: ultrastrong light-matter coupling and slow-down of light," *Phys. Rev. B* **85**, 081302 (2012).
34. C. Poellmann, P. Steinleitner, U. Leierseder, P. Nagler, G. Plechinger, M. Porer, R. Bratschitsch, C. Schüller, T. Korn, and R. Huber, "Resonant internal quantum transitions and femtosecond radiative decay of excitons in monolayer  $\text{WSe}_2$ ," *Nat. Mater.* **14**, 889–893 (2015).
35. D. Turchinovich, F. D'Angelo, and M. Bonn, "Femtosecond-timescale buildup of electron mobility in GaAs observed via ultrabroadband transient terahertz spectroscopy," *Appl. Phys. Lett.* **110**, 121102 (2017).
36. T. Yu and Y. Lu, "Intervalley scattering in GaAs(111)-supported silicene," *Phys. Chem. Chem. Phys.* **22**, 26402–26409 (2020).
37. W. P. D. Wong, J. Yin, B. Chaudhary, X. Y. Chin, D. Cortecchia, S.-Z. A. Lo, A. C. Grimsdale, O. F. Mohammed, G. Lanzani, and C. Soci, "Large polaron self-trapped states in three-dimensional metal-halide perovskites," *ACS Mater. Lett.* **2**, 20–27 (2020).
38. F. Ganikhanov, K. C. Burr, and C. L. Tang, "Ultrafast dynamics of holes in GaAs probed by two-color femtosecond spectroscopy," *Appl. Phys. Lett.* **73**, 64–66 (1998).
39. Z. E. Eroglu, O. Comegys, L. S. Quintanar, N. Azam, S. Elafandi, M. Mahjouri-Samani, and A. Boulesbaa, "Ultrafast dynamics of exciton formation and decay in two-dimensional tungsten disulfide ( $2\text{D-WSe}_2$ ) monolayers," *Phys. Chem. Chem. Phys.* **22**, 17385–17393 (2020).
40. H. Chen, X. Wen, J. Zhang, T. Wu, Y. Gong, X. Zhang, J. Yuan, C. Yi, J. Lou, P. M. Ajayan, W. Zhuang, G. Zhang, and J. Zheng, "Ultrafast formation of interlayer hot excitons in atomically thin  $\text{MoS}_2/\text{WS}_2$  heterostructures," *Nat. Commun.* **7**, 12512 (2016).
41. S. Cha, J. H. Sung, S. Sim, J. Park, H. Heo, M.-H. Jo, and H. Choi, "1s-intraexcitonic dynamics in monolayer  $\text{MoS}_2$  probed by ultrafast mid-infrared spectroscopy," *Nat. Commun.* **7**, 10768 (2016).
42. A. S. Kowlig, H. Timmers, A. J. Lind, U. Elu, F. C. Cruz, P. G. Schunemann, J. Biegert, and S. A. Diddams, "Infrared electric field sampled frequency comb spectroscopy," *Sci. Adv.* **5**, eaaw8794 (2019).
43. C. R. Baiz, B. Blasiak, J. Bredenbeck, M. Cho, J.-H. Choi, S. A. Corcelli, A. G. Dijkstra, C.-J. Feng, S. Garrett-Roe, N.-H. Ge, M. W. D. Hanson-Heine, J. D. Hirst, T. L. C. Jansen, K. Kwac, K. J. Kubarych, C. H. Londergan, H. Maekawa, M. Reppert, S. Saito, S. Roy, J. L. Skinner, G. Stock, J. E. Straub, M. C. Thielges, K. Tominaga, A. Tokmakoff, H. Torii, L. Wang, L. J. Webb, and M. T. Zanni, "Vibrational spectroscopic map, vibrational spectroscopy, and intermolecular interaction," *Chem. Rev.* **120**, 7152–7218 (2020).
44. M. Maj, C. Ahn, D. Kossowska, K. Park, K. Kwak, H. Han, and M. Cho, "Beta-isocyanoalanine as an IR probe: comparison of vibrational dynamics between isonitrile and nitrile-derivatized IR probes," *Phys. Chem. Chem. Phys.* **17**, 11770–11778 (2015).
45. M. Di Donato and M. L. Groot, "Ultrafast infrared spectroscopy in photosynthesis," *Biochim. Biophys. Acta Bioenergetics* **1847**, 2–11 (2015).
46. B. Xiang, Y. Li, C. H. Pham, F. Paesani, and W. Xiong, "Ultrafast direct electron transfer at organic semiconductor and metal interfaces," *Sci. Adv.* **3**, e1701508 (2017).
47. A. A. Bakulin, R. Lovrincic, X. Yu, O. Selig, H. J. Bakker, Y. L. A. Rezus, P. K. Nayak, A. Fonari, V. Coropceanu, J.-L. Brédas, and D. Cahen,

- "Mode-selective vibrational modulation of charge transport in organic electronic devices," *Nat. Commun.* **6**, 7880 (2015).
48. T. Zentgraf, R. Huber, N. C. Nielsen, D. S. Chemla, and R. A. Kaindl, "Ultrabroadband 50–130 thz pulses generated via phase-matched difference frequency mixing in  $\text{LiIO}_3$ ," *Opt. Express* **15**, 5775–5781 (2007).
49. K. Kato, "High-power difference-frequency generation at 5–11  $\mu\text{m}$  in  $\text{AgGaAs}_2$ ," *IEEE J. Quantum Electron.* **20**, 698–699 (1984).
50. P. Tidemand-Lichtenberg, J. S. Dam, H. V. Andersen, L. Høgstedt, and C. Pedersen, "Mid-infrared upconversion spectroscopy," *J. Opt. Soc. Am. B* **33**, D28–D35 (2016).
51. J. Zhu, T. Mathes, A. D. Stahl, J. T. Kennis, and M. L. Groot, "Ultrafast mid-infrared spectroscopy by chirped pulse upconversion in 1800–1000  $\text{cm}^{-1}$  region," *Opt. Express* **20**, 10562–10571 (2012).
52. H. J. Bakker, G. C. Cho, H. Kurz, Q. Wu, and X.-C. Zhang, "Distortion of terahertz pulses in electro-optic sampling," *J. Opt. Soc. Am. B* **15**, 1795–1801 (1998).
53. M. C. Beard, G. M. Turner, and C. A. Schmuttenmaer, "Subpicosecond carrier dynamics in low-temperature grown GaAs as measured by time-resolved terahertz spectroscopy," *J. Appl. Phys.* **90**, 5915–5923 (2001).
54. D. Polli, D. Brida, S. Mukamel, G. Lanzani, and G. Cerullo, "Effective temporal resolution in pump-probe spectroscopy with strongly chirped pulses," *Phys. Rev. A* **82**, 053809 (2010).
55. M. C. Beard, G. M. Turner, and C. A. Schmuttenmaer, "Transient photoconductivity in GaAs as measured by time-resolved terahertz spectroscopy," *Phys. Rev. B* **62**, 15764–15777 (2000).
56. M. Wickenhauser, J. Burgdörfer, F. Krausz, and M. Drescher, "Time resolved Fano resonances," *Phys. Rev. Lett.* **94**, 023002 (2005).
57. L. Argenti, R. Pazourek, J. Feist, S. Nagele, M. Liertzer, E. Persson, J. Burgdörfer, and E. Lindroth, "Photoionization of helium by attosecond pulses: extraction of spectra from correlated wave functions," *Phys. Rev. A* **87**, 053405 (2013).
58. V. Gruson, L. Barreau, Á. Jiménez-Galan, F. Risoud, J. Caillat, A. Maquet, B. Carré, F. Lepetit, J.-F. Hergott, T. Ruchon, L. Argenti, R. Taeb, F. Martn, and P. Salières, "Attosecond dynamics through a Fano resonance: monitoring the birth of a photoelectron," *Science* **354**, 734–738 (2016).
59. A. Kaldun, A. Blättermann, V. Stooß, S. Donsa, H. Wei, R. Pazourek, S. Nagele, C. Ott, C. D. Lin, J. Burgdörfer, and T. Pfeifer, "Observing the ultrafast buildup of a Fano resonance in the time domain," *Science* **354**, 738–741 (2016).
60. D. W. Bailey and C. J. Stanton, "Calculations of femtosecond differential optical transmission in germanium," *J. Appl. Phys.* **77**, 2107–2115 (1995).
61. A. Dargys and J. Kundrotas, *Handbook on Physical Properties of Ge, Si, GaAs and InP* (Science and Encyclopedia Publ., 1994).
62. F. Meng, M. D. Thomson, B. E. Sernelius, M. Jörger, and H. G. Roskos, "Ultrafast dynamic conductivity and scattering rate saturation of photoexcited charge carriers in silicon investigated with a midinfrared continuum probe," *Phys. Rev. B* **91**, 075201 (2015).
63. B. E. Sernelius, "Intraband relaxation time in highly excited semiconductors," *Phys. Rev. B* **43**, 7136–7144 (1991).
64. M. Bernardi, D. Vigil-Fowler, C. S. Ong, J. B. Neaton, and S. G. Louie, "Ab initio study of hot electrons in GaAs," *Proc. Natl. Acad. Sci. USA* **112**, 5291–5296 (2015).
65. T. Terashige, H. Yada, Y. Matsui, T. Miyamoto, N. Kida, and H. Okamoto, "Temperature and carrier-density dependence of electron-hole scattering in silicon investigated by optical-pump terahertz-probe spectroscopy," *Phys. Rev. B* **91**, 241201 (2015).
66. I. Floss, C. Lemell, G. Wachter, V. Smejkal, S. A. Sato, X.-M. Tong, K. Yabana, and J. Burgdörfer, "Ab initio multiscale simulation of high-order harmonic generation in solids," *Phys. Rev. A* **97**, 011401 (2018).
67. I. Floss, C. Lemell, K. Yabana, and J. Burgdörfer, "Incorporating decoherence into solid-state time-dependent density functional theory," *Phys. Rev. B* **99**, 224301 (2019).